Exploration of Multi-Component Vanadium and Titanium Pnictides Using Flux Growth and Conventional High-Temperature Methods

Alexander Ovchinnikov [1,2] and Svilen Bobev [1]*

[1] Department of Chemistry and Biochemistry, University of Delaware, Newark, DE, United States, [2] Department of Materials and Environmental Chemistry, Stockholm University, Stockholm, Sweden

The flux growth method was successfully employed to synthesize millimeter-sized single crystals of the ternary barium vanadium pnictides $Ba_5V_{12}As_{19+x}$ ($x \approx 0.02$) and $Ba_5V_{12}Sb_{19+x}$ ($x \approx 0.36$), using molten Pb and Sb, respectively. Both compositions crystallize in space group $P\bar{4}3m$ and adopt a structure similar to those of the barium titanium pnictides $Ba_5Ti_{12}Pn_{19+x}$ (Pn = Sb, Bi), yet with a subtly different disorder, involving the pnictogen and barium atoms. Attempts to obtain an arsenide analog of $Ba_5Ti_{12}Pn_{19+x}$ using a Pb flux technique yielded binary arsenides. High-temperature treatment of the elements Ba, Ti, and As in Nb or Ta tubes resulted in side reactions with the crucible materials and produced two isostructural compositions $Ba_8Ti_{13-x}M_xAs_{21}$ (M = Nb, Ta; $x \approx 4$), representing a new structure type. The latter structure displays fcc-type metal clusters comprised of statistically distributed Ti and M atoms (M = Nb, Ta) with multi-center and two-center bonding within the clusters, as suggested by our first-principle calculations.

Keywords: flux growth, pnictides, crystal structure, electronic structure, metal clusters

INTRODUCTION

The application of molten metals as inert or reactive solvents for the crystal growth of intermetallic compounds is an actively used synthetic approach in solid-state chemistry. In a typical flux growth experiment, a mixture of selected metallic elements, along with a suitable flux material (also a metal or eutectic mixture of metals) are loaded in an inert container (graphite, alumina or other refractory materials, or high-melting metals from groups 5 or 6, such as Nb, Ta, and Mo). The reaction container can be equipped with some sort of filter or sieve for separating the molten flux from the grown crystals (Canfield and Fisk, 1992; Kanatzidis et al., 2005; Latturner, 2018). The as-prepared mixtures are then heated up, typically well above the melting point of the flux to achieve reasonably high diffusion rates and solubility. In general, complete dissolution is not necessary for production of small crystals, suitable for, e.g., single-crystal X-ray diffraction. However, obtaining larger crystals, which can be utilized for accurate physical property measurements, usually requires precipitation from homogeneous melts to assure a small number of crystallization centers (Wolff and Mlavsky, 1974). After the homogenization step, the temperature is lowered to allow formation of a solid phase. The flux material can then be removed by inverting the reactor at a temperature above the flux melting point and letting the molten flux pass through the filter, leaving the grown crystals behind. Alternatively, selective etching or evaporation of the flux can be used to recover the

crystals from the reaction batch. In certain cases, single crystals can be mechanically isolated after breaking the solidified product (Canfield and Fisk, 1992; Kanatzidis et al., 2005). An important point that has to be taken into account when growing single crystals via the flux growth method is possible undesirable incorporation of the flux material into the crystal structure of the produced crystals. In such instances, the observed crystal structure may be inherently flux-stabilized and cannot be reproduced in a flux-free environment (Khan et al., 2018; Felder et al., 2019).

The flux growth process is well-suited for the production of incongruently-melting materials, but it can also be efficient for the growth of congruently-melting compounds when their melting points are prohibitory high. Since ternary and higher multicomponent phase diagrams are usually unknown, making the information about melting temperatures as well as phase relationships inaccessible, the flux method, owing to its wide applicability, offers a tool for explorative search for new materials. Various classes of intermetallics have been prepared by this route. In particular, numerous ternary (Ovchinnikov et al., 2017b; Baranets et al., 2019a; Childs et al., 2019; Nakamura et al., 2019; Ovchinnikov and Bobev, 2019a), quaternary (Ovchinnikov et al., 2017a, 2018a; Baranets and Bobev, 2019; Baranets et al., 2019b; Jayasinghe et al., 2019; Wakiya et al., 2019), and even quinary (Zaikina et al., 2010, 2017; Ma et al., 2012) compositions were successfully synthesized in the form of single crystals. Some examples of complex intermetallics which have been recently produced from metal fluxes include $AE_3Ti_8Bi_{10}$ (Ovchinnikov and Bobev, 2019b), $AELi_2In_2Ge_2$ (AE = Sr, Ba, Eu) (Ovchinnikov and Bobev, 2019c), $Y_7Ru_4InGe_{12}$ (Bao et al., 2019), and $R_5Mg_5Fe_4Al_xSi_{18-x}$ (R = Gd, Dy, Y) (Ma et al., 2012).

Even apparently well-established binary systems may sometimes yield surprising new compositions, as it was the case for the RE–Bi (RE = Nd, Sm) systems (Ovchinnikov et al., 2018b), which host the isostructural RE_3Bi_7 phases, overlooked in the multiple early assessments of the corresponding phase diagrams. Careful optimization of the flux growth procedure resulted in large single crystals of these recently discovered compounds.

In this contribution, we explored the application of the metal flux approach to the synthesis of multinary vanadium pnictides. The choice of the elements was in part motivated by the lack of detailed experimental data on the ternary compounds in the A–V–Pn systems, where A stands for an electropositive metal, such as alkali, alkaline-earth, or rare-earth metal, and Pn is pnictogen, i.e., a group 15 element. From the physical property perspective, some of the early transition metal pnictides were reported to display interesting electronic behavior, such as superconductivity in $K_2Cr_3As_3$ (Bao et al., 2015) and doped $BaTi_2Sb_2O$ (Doan et al., 2012), and itinerant ferromagnetism in $LaCrSb_3$ (Raju et al., 1998). In addition, our recent exploratory work in the field of titanium pnictides revealed several new phases in the AE–Ti–Bi systems (AE = Ca, Sr, Ba, Eu) (Ovchinnikov and Bobev, 2018a, 2019b). Taking into account pronounced structural similarities between multinary titanium and vanadium pnictides (Brylak and Jeitschko, 1994; Bie and Mar, 2009; Failamani et al., 2015; Ovchinnikov and Bobev, 2018a), the existence of yet unknown multinary vanadium pnictides can be foreseen.

We focused our studies on the ternary arsenides and antimonides of vanadium with alkaline-earth metals. Due to extremely low solubility of V in liquid Bi and the lack of stable binary bismuthides, Bi was excluded from our consideration, although it is conceivable that with suitably modified synthetic protocols, analogous bismuthides could also be found. The exploratory search resulted in two ternaries, $Ba_5V_{12}As_{19+x}$ ($x \approx 0.02$) and $Ba_5V_{12}Sb_{19+x}$ ($x \approx 0.36$), grown from liquid Pb and Sb, respectively. By high-temperature treatment of the elemental mixture with the nominal composition "$Ba_5Ti_{12}As_{19}$" in Nb or Ta tubes, new isostructural compounds with the general formula $Ba_8Ti_{13-x}M_xAs_{21}$ (M = Nb, Ta) were produced. A striking structural peculiarity of these phases, adopting a new structure type, is the presence of fcc-type transition metal clusters with pronounced multi-center, as well as two-center, bonding.

EXPERIMENTAL

Synthesis

Due to the air-sensitivity of the starting materials and the final products, most operations were performed in an argon-filled glovebox. All used materials had stated purity of at least 99.9 wt. %. Flux-assisted single crystal growth was employed for the synthesis of $Ba_5V_{12}As_{19.02(1)}$ and $Ba_5V_{12}Sb_{19.36(2)}$. For the former compound, metallic Pb was utilized as a flux. A mixture of Ba, V, As, and Pb with a molar ratio of 2:1:4:25, respectively, was placed in an alumina crucible topped with a piece of quartz wool and sealed in an evacuated fused silica tube. The reactor was heated up to 1173 K in a box furnace with a rate of 200 K/h. After the mixture was allowed to homogenize for 48 h, it was cooled down to 823 K with a rate of 5 K/h. At this final temperature, the fused silica tube was removed from the furnace, inverted, and subjected to centrifugation. The molten lead seeped through the quartz wool leaving the crystallized product on the wool and inside the crucible. The tube was break-opened inside the glovebox and the solid material was mechanically collected and inspected under an optical microscope. Besides some inhomogeneously looking powder, which was revealed by powder X-ray diffraction to be a mixture of binary Ba and V arsenides, well-formed single crystals of isotropic polyhedral shape and dimensions up to 1 mm were clearly visible. These crystals turned out to be a new compound with the composition $Ba_5V_{12}As_{19.02(1)}$ as was determined by single-crystal X-ray diffraction.

The single crystal growth of $Ba_5V_{12}Sb_{19.36(2)}$ was carried out applying a Sb self-flux approach. A similar experimental setup was used as detailed above. The starting mixture consisted of Ba, V, and Sb in a molar ratio of 2:1:4, respectively. The reactor was heated up to 1273 K with a rate of 50 K/h and kept at this temperature for 48 h. After that, the temperature was lowered to 1023 K with a rate of 5 K/h, and the excess of Sb was removed by centrifugation. Large crystals with dimensions up to 4–5 mm were the only solid product found in the crucible. Powder and single crystal X-ray diffraction analysis showed that the product was single phase $Ba_5V_{12}Sb_{19.36(2)}$.

Crystals of the new quaternary compound $Ba_8Ti_{9.24(6)}Ta_{3.76}As_{21}$ were discovered in the sample prepared by a direct reaction of the elements with the targeted composition

$Ba_5Ti_{12}As_{19}$. The starting mixture was placed in a weld-shut Ta tube under protective high-purity Ar atmosphere and sealed in an evacuated fused silica tube, which was subsequently loaded in a tube furnace. One end of the tube was left protruding out from the furnace to keep this part of the reactor at room temperature, as a safety measure: in the case of the Ta tube failure, the toxic As vapor would condense on the cold end without building dangerously high pressure inside the silica tube. The tube was heated up to 1273 K with a rate of 200 K/h, annealed at this temperature for 48 h, and cooled down to room temperature with a rate of 5 K/h. The resulting sample mostly consisted of binary Ba and Ti arsenides according to powder X-ray diffraction. However, strong peaks belonging to an unidentified phase were evident in the powder patterns. Visual inspection of the product under a microscope revealed the presence of single crystals with different morphologies. Among them, small submillimeter-sized crystals with cubic or octahedral shape could be easily distinguished. Subsequent single crystal data collection and refinement confirmed a new structure with the chemical formula $Ba_8Ti_{9.24(6)}Ta_{3.76}As_{21}$. The Ta in the composition obviously originated from the reactor. To indirectly cross check the results of the structural refinement, the reaction was repeated using the same protocol as described above, but in a Nb tube instead of Ta. The outcome of the synthesis with respect to the major phases was similar to the previous attempt. Single crystals with the refined composition $Ba_8Ti_{9.0(3)}Nb_{4.0}As_{21}$, isotypic with the Ta-containing phase, were found as a side product, thus confirming the crystal structure.

Powder X-Ray Diffraction (PXRD)

Powder X-ray diffraction measurements were done in the reflection mode on a Rigaku Miniflex diffractometer (Cu K$_\alpha$ radiation $\lambda = 1.5418$ Å) operating inside a nitrogen-filled glovebox to prevent sample deterioration upon contact with the ambient atmosphere. The powder patterns were recorded in a $\Theta-\Theta$ scan mode with a step size of 0.05° and a 2 s per step acquisition time.

Single-Crystal X-Ray Diffraction

Suitable single crystals were selected and cut to desired dimensions under dry Paratone N oil using low-background plastic loops. Data were recorded in a cold nitrogen stream at $T = 200$ K on a Bruker SMART APEX CCD diffractometer equipped with monochromated Mo K$_\alpha$ radiation ($\lambda = 0.71073$ Å). The raw data were integrated using the program SAINT (SAINT, 2014). Semiempirical absorption corrections were performed with the SADABS software (SADABS, 2014). Crystal structures were solved by dual-space methods with SHELXT (Sheldrick, 2015a) and refined by full matrix least-squares methods on F^2 using SHELXL (Sheldrick, 2015b). All studied compounds showed a certain degree of crystallographic disorder. Assignment of chemical types was straightforward, based on the interatomic distances and coordination environments. Atomic coordinates were standardized using STRUCTURE TIDY (Gelato and Parthé, 1987). Details of the data collection, crystallographic parameters, and selected interatomic distances are summarized in **Tables 1–6**.

First-Principle Calculations

For electronic structure calculations, a hypothetical disorder-free $Ba_5V_{12}As_{19}$ model was employed. The split Ba1 site was treated as a single position with averaged atomic coordinates, and the partially occupied As6 and As7 sites were removed. An ordered model was also generated for $Ba_8Ti_{9.0(3)}Nb_{4.0}As_{21}$. For this purpose, the experimentally determined $Fm\bar{3}m$ structure was transformed into a $I4/mmm$ subgroup with half the original unit cell volume and the following transformation of the transition metal sites: $4a \rightarrow 2a$, $48h \rightarrow 16m + 8i$. The Nb atoms were placed exclusively in the $8i$ positions, resulting in the formula $Ba_8Ti_9Nb_4As_{21}$.

The calculations were executed with the TB-LMTO-ASA package (Jepsen and Andersen, 2000) at the local density approximation level applying the von Barth-Hedin exchange-correlation functional (von Barth and Hedin, 1972). Empty spheres were added to satisfy the Atomic Sphere Approximation (ASA). Chemical bonding was examined using Crystal Orbital Hamilton Population curves (COHP) (Steinberg and Dronskowski, 2018) and Electron Localization Function (ELF) (Savin et al., 1997), evaluated by the respective modules of the LMTO package. Electron density was integrated using the program Critic2 (Otero-de-la-Roza et al., 2014).

DISCUSSION

Synthesis

The use of Pb as a flux for the synthesis of arsenides provides considerable benefits over the high-temperature annealing of the elements. High solubilities of many elements in molten Pb and its low melting point enable single crystal growth at moderately high temperatures, without significant losses of the highly volatile As. In addition, owing to their dilution, the dissolved starting materials in the course of a flux growth process display reduced chemical activity toward the reaction container, thereby preventing side reactions, which are often inevitable in the conventional high-temperature approach (Chen and Corbett, 2004; Baranets et al., 2018). A particular advantage of the flux approach is the possibility to produce single crystals containing elements with significantly different melting points, providing that all of the elements are reasonably soluble in the flux. We applied this approach to synthesize new multinary vanadium arsenides, since in this case, too, the high melting point of V (T_m = 2183 K) and the low sublimation point of As (T_{subl} = 883 K) make direct synthesis from the elements rather challenging.

Among the compositions in the AE–V–As–Pb systems (AE = Ca, Sr, Ba) used for single crystal growth attempts, only experiments with AE = Ba produced a new ternary phase, $Ba_5V_{12}As_{19+x}$. For AE = Ca and Sr, binary arsenides were detected as products in all reactions. Although $Ba_5V_{12}As_{19+x}$ can be obtained from different starting elemental ratios, so far it has been observed as a side product, indicating that further optimization of the procedure is necessary. In all cases, binary metal arsenides have been detected alongside $Ba_5V_{12}As_{19+x}$. The low yield of $Ba_5V_{12}As_{19+x}$ is suggestive that the reaction conditions used for AE = Ca and Sr may also be improved to ultimately afford ternary compounds. Due to high reactivity

TABLE 1 | Data collection details and selected crystallographic data ($T = 200$ K, Mo K$_\alpha$, $\lambda = 0.71073$ Å).

Refined composition	$Ba_5V_{12}As_{19.02(1)}$	$Ba_5V_{12}Sb_{19.36(2)}$	$Ba_8Ti_{9.0(3)}Nb_{4.0}As_{21}$	$Ba_8Ti_{9.24(6)}Ta_{3.76}As_{21}$
fw/ g mol^{-1}	2722.96	3655.06	3474.22	3795.01
Space group	$P\bar{4}3m$	$P\bar{4}3m$	$Fm\bar{3}m$	$Fm\bar{3}m$
Z	2	2	4	4
a/ Å	11.398 (1)	12.125 (1)	15.684 (7)	15.691 (3)
V/ Å^3	1480.8 (5)	1782.7 (5)	3858 (5)	3863 (2)
ρ_{calc}/ g cm^{-3}	6.11	6.81	5.98	6.52
$\mu_{MoK\alpha}$/ cm^{-1}	312.0	227.5	287.7	382.3
R$_1$ [$I > 2\sigma(I)$][a]	0.025	0.021	0.036	0.025
wR$_2$ [$I > 2\sigma(I)$][a]	0.054	0.043	0.080	0.065
R$_1$ [all data][a]	0.027	0.022	0.050	0.028
wR$_2$ [all data][a]	0.055	0.043	0.083	0.066
Flack's parameter	0.06 (2)	−0.03 (7)	—	—
$\Delta\rho_{max,min}$/ e Å^{-3}	0.69−1.41	0.80−0.91	1.29−1.07	1.85−1.38

[a]$R_1 = \sum||F_o|-|F_c||/\sum|F_o|$; $wR_2 = [\sum[w(F_o^2-F_c^2)^2]/\sum[w(F_o^2)^2]]^{1/2}$, where $w = 1/[\sigma^2 F_o^2 + (AP)^2 + (BP)]$, and $P = (F_o^2 + 2F_c^2)/3$; A, B are the respective weight coefficients as in the corresponding CIFs (depository numbers 1959265-1959268).

of As toward various metals used as container materials in high-temperature reactions, systematic studies of the potential homogeneity range in $Ba_5V_{12}As_{19+x}$ have been obstructed by side-reactions. However we would like to note that our investigations in the AE–Ti–Bi systems (AE = Sr, Ba), which host structurally related $AE_5Ti_{12}Bi_{19+x}$ compounds, revealed that the Bi content depends on the alkaline-earth metal chosen, but the respective homogeneity ranges for a given AE were found to be rather narrow (Ovchinnikov and Bobev, 2018a).

The relatively low melting point of Sb ($T_m = 903$ K) allows its application as a reactive flux for the synthesis of antimonides. Such "self-flux" approach prevents potential contamination of the grown crystals by foreign elements. Crystal growth attempts in the Ba–V–Sb system yielded well-formed single crystals of $Ba_5V_{12}Sb_{19.36(2)}$. It is worthwhile to mention that a very similar composition was found for the ternary Ba–V–Sb phase prepared by high-temperature annealing of an arc-melted sample with the nominal composition ≈ Ba5V12Sb25 (Failamani et al., 2015), suggesting that the obtained crystals are on the Sb-rich side of the homogeneity range. The crystal structure reported in Failamani et al. (2015) was refined as a Ba-deficient $Ba_{5-\delta}V_{12}Sb_{19+x}$. Our refinement does not provide evidence for any Ba vacancies but confirms the previously described splitting of the Ba site. Furthermore, this splitting is correlated with the disorder in the Sb substructure.

To date, flux growth experiments in the Sr–V–Sb system have resulted in binary antimonides only. In the Ca–V–Sb system, the exploratory work so far has resulted in the phase CaV_3Sb_4 (Ovchinnikov and Bobev, 2020), which is structurally unrelated to $Ba_5V_{12}Sb_{19+x}$.

Crystal growth experiments in the AE–Ti–As–Pb systems (AE = Ca, Sr, Ba) always produced binary arsenides. Since the ternary compounds $Ba_5Ti_{12}Pn_{19+x}$ (Pn = Sb, Bi), structurally related to $Ba_5V_{12}Pn_{19+x}$ (Pn = As, Sb), have been synthesized and characterized in detail (Bie and Mar, 2009; Ovchinnikov and Bobev, 2018a; Han et al., 2019), it may seem surprising

TABLE 2 | Atomic coordinates and equivalent isotropic displacement parameters for $Ba_5V_{12}As_{19.02(1)}$.

Atom	Site	x	y	z	U_{eq}^a (Å^2)
Ba1A[b]	6g	0.1754 (3)	1/2	1/2	0.0109 (4)
Ba1B[b]	6g	0.208 (2)	1/2	1/2	0.0109 (4)
Ba2	4e	0.83313 (7)	x	x	0.0108 (3)
V1	12i	0.1576 (1)	x	0.3240 (2)	0.0081 (4)
V2	12h	0.1910 (2)	1/2	0	0.0073 (4)
As1	12i	0.21596 (8)	x	0.5341 (1)	0.0100 (3)
As2	12i	0.32944 (8)	x	0.0124 (1)	0.0079 (3)
As3	6f	0.3724 (2)	0	0	0.0076 (4)
As4[b]	4e	0.1123 (1)	x	x	0.0085 (6)
As5	4e	0.3145 (1)	x	x	0.0105 (5)
As6[b]	1b	1/2	1/2	1/2	0.010[c]
As7[b]	1a	0	0	0	0.010[c]

[a]U_{eq} is defined as one third of the trace of the orthogonalized U_{ij} tensor. [b]Refined occupancies, occ(Ba1A) = 0.90(1), occ(Ba1B) = 1 − occ(Ba1A), occ(As4) = 1 − occ(As7), occ(As6) = 1 − occ(Ba1A), occ(As7) = 0.020(7). [c]For As6 and As7, displacement parameters were refined isotropically and were constrained to the equivalent value U_{eq} of As5[1].

that the isoelectronic "$Ba_5Ti_{12}As_{19+x}$" could not be obtained. To address this issue, we attempted the synthesis of this nominal

---

[1]During the refinement of the $Ba_5V_{12}As_{19.02(1)}$ structure, a considerable residual electron density was detected in the corners of the unit cell. Modifications of the absorption correction did not result in disappearance of this feature. The only chemical species which would show reasonable local coordination when placed in this position was As. After ascribing the observed density peak to As (labeled here As7), the resulting Ba–As contacts were within the distance range found for other bonds of this sort in the structure. The refined occupancy of As7 was only about 2 %. Owing to an unphysically short As7–As4 distance of 2.217(1) Å, the occupancy of As4 was set to 100 − occupancy(As7) %. Acknowledging the possibility that the observed residual density peak is an artifact of the special position, we abstain from the discussion of this disorder until additional data are available. Due to the very small occupancy, the effect of the As7 site on the structure and composition is negligible.

TABLE 3 | Atomic coordinates and equivalent isotropic displacement parameters for $Ba_5V_{12}Sb_{19.36(2)}$.

Atom	Site	x	y	z	U_{eq}^{a} (Å²)
Ba1A[b]	6g	0.176 (1)	1/2	1/2	0.019 (2)[c]
Ba1B[b]	6g	0.205 (1)	1/2	1/2	0.0192[c]
Ba2	4e	0.83409 (8)	x	x	0.0143 (3)
V1	12i	0.1577 (2)	x	0.3251 (2)	0.0102 (5)
V2	12h	0.1869 (2)	1/2	0	0.0092 (5)
Sb1	12i	0.21688 (5)	x	0.54212 (8)	0.0111 (2)
Sb2	12i	0.33244 (6)	x	0.01314 (8)	0.0096 (2)
Sb3	6f	0.3653 (1)	0	0	0.0085 (3)
Sb4	4e	0.11037 (8)	x	x	0.0112 (4)[c]
Sb5	4e	0.31655 (8)	x	x	0.0113 (4)
Sb6A[b]	1b	1/2	1/2	1/2	0.018 (3)
Sb7[b]	4e	0.459 (1)	x	x	0.0112[c]

[a]U_{eq} is defined as one third of the trace of the orthogonalized U_{ij} tensor. [b]Refined occupancies, occ(Ba1A) = 0.57(2), occ(Ba1B) = 1 – occ(Ba1A), occ(Sb6A) = 1 – occ(Ba1A), occ(Sb7) = 0.071(4). [c]Within the atomic pairs Ba1A and Ba1B and Sb4 and Sb7, respectively, anisotropic displacement parameters were constrained to be equal.

TABLE 4 | Atomic coordinates and equivalent isotropic displacement parameters for $Ba_8Ti_{13-x}M_xAs_{21}$ (M = Nb, Ta).

Atom	Site	x	y	z	U_{eq}^{a} (Å²)
$Ba_8Ti_{9.0(3)}Nb_{4.0}As_{21}$					
Ba1	32f	0.36972 (5)	x	x	0.0144 (4)
Ti/Nb1[b]	48h	0	0.1388 (1)	y	0.0116 (8)
Ti/Nb2[b]	4a	0	0	0	0.017 (2)
As1	32f	0.16332 (8)	x	x	0.0160 (6)
As2	24e	0.2306 (2)	0	0	0.0126 (6)
As3	24d	0	1/4	1/4	0.0126 (6)
As4	4b	1/2	1/2	1/2	0.015 (1)
$Ba_8Ti_{9.24(6)}Ta_{3.76}As_{21}$					
Ba1	32f	0.36964 (3)	x	x	0.0135 (3)
Ti/Ta1[c]	48h	0	0.13858 (5)	y	0.0122 (4)
Ti/Ta2[c]	4a	0	0	0	0.016 (2)
As1	32f	0.16325 (5)	x	x	0.0145 (4)
As2	24e	0.2306 (1)	0	0	0.0124 (4)
As3	24d	0	1/4	1/4	0.0123 (4)
As4	4b	1/2	1/2	1/2	0.0135 (9)

[a]U_{eq} is defined as one third of the trace of the orthogonalized U_{ij} tensor. [b]Ti/Nb1 = 0.73(2)Ti + 0.27Nb, Ti/Nb2 = 0.29(5)Ti + 0.71Nb. [c]Ti/Ta1 = 0.703(4)Ti + 0.297Ta, Ti/Ta2 = 0.81(1)Ti + 0.19Ta.

composition in Nb and Ta tubes, as described in the Experimental section. Synthesis of arsenides in metal containers is often complicated by possible side reactions with the reactor walls. As a matter of fact, many new compounds were originally discovered as unexpected outcomes of such reactions (He et al., 2012; Baranets et al., 2018). Although the desired $Ba_5Ti_{12}As_{19+x}$ was not detected in the products extracted from the Nb and Ta tubes after the high-temperature treatment, two isostructural compositions representing a new structure type were obtained – $Ba_8Ti_{9.0(3)}Nb_{4.0}As_{21}$ and $Ba_8Ti_{9.24(6)}Ta_{3.76}As_{21}$.

TABLE 5 | Selected interatomic distances in $Ba_5V_{12}Pn_{19+x}$ (Pn = As, Sb).

Atoms		Distance (Å)	
		$Ba_5V_{12}As_{19.02(1)}$	$Ba_5V_{12}Sb_{19.36(2)}$
Ba1A	$-Pn1 \times 4$	3.2933 (9)	3.506 (2)
	$-Pn2 \times 2$	3.318 (2)	3.485 (7)
	$-Pn5 \times 2$	3.384 (2)	3.579 (6)
	$-Pn2 \times 2$	3.484 (2)	3.675 (8)
	$-Pn7 \times 2$	–	3.50 (1)
Ba1B	$-Pn5 \times 2$	3.226 (8)	3.424 (5)
	$-Pn1 \times 4$	3.262 (1)	3.4737 (9)
	$-Pn6$	3.33 (2)	3.58 (1)
	$-Pn2 \times 2$	3.54 (1)	3.698 (8)
Ba2	$-Pn7$	3.294 (1)	–
	$-Pn4 \times 3$	3.301 (1)	3.483 (2)
	$-Pn2 \times 3$	3.323 (2)	3.587 (1)
	$-Pn1 \times 3$	3.499 (2)	3.647 (2)
	$-Pn3 \times 3$	3.567 (1)	3.734 (1)
V1	$-Pn4$	2.521 (3)	2.728 (3)
	$-Pn5$	2.531 (3)	2.726 (3)
	$-Pn2 \times 2$	2.565 (1)	2.7513 (8)
	$-Pn1$	2.573 (3)	2.820 (3)
	$-Pn3$	2.600 (2)	2.748 (2)
	$-V1 \times 2$	2.682 (4)	2.871 (4)
	$-V2 \times 2$	2.720 (2)	2.877 (2)
V2	$-Pn2 \times 2$	2.508 (1)	2.696 (2)
	$-Pn1 \times 2$	2.508 (1)	2.7033 (8)
	$-Pn3 \times 2$	2.618 (2)	2.793 (2)
	$-V1 \times 2$	2.720 (2)	2.877 (2)
	$-V2 \times 2$	3.078 (3)	3.205 (3)
Pn3	$-Pn3$	2.910 (4)	3.266 (3)
Pn5	$-Pn1 \times 3$	2.965 (1)	3.2252 (9)
	$-Pn7$	–	2.98 (3)

Structure

$Ba_5V_{12}Pn_{19+x}$ (Pn = As, Sb). The crystal structures of $Ba_5V_{12}As_{19.02(1)}$ and $Ba_5V_{12}Sb_{19.36(2)}$ are closely related to each other and to those of the Ti-antimonide $Ba_5Ti_{12}Sb_{19+x}$ (Bie and Mar, 2009) and Ti-bismuthide $AE_5Ti_{12}Bi_{19+x}$ (AE = Sr, Ba) ternaries (Ovchinnikov and Bobev, 2018a). Subtle structural variations are associated with different realization of disorder in the Pn sites. Similarly to $Ba_5Ti_{12}Sb_{19+x}$ and $AE_5Ti_{12}Bi_{19+x}$ (AE = Sr, Ba), $Ba_5V_{12}Pn_{19+x}$ (Pn = As, Sb) crystallize in the noncentrosymmetric space group $P\bar{4}3m$, with Pearson code cP72 (excluding the partially occupied sites). Refined Flack's parameter was close to zero for both compositions confirming correctness of the absolute configuration.

Analogously to the related Ti pnictides, in $Ba_5V_{12}Pn_{19+x}$ (Pn = As, Sb), the deficiency-free part of the Ba–Pn substructure resembles a γ-brass-type framework (**Figure 1A**). The nested 26-atom cluster centered around the unit cell corner can be described as two interpenetrating Ba_4 and Pn_4 tetrahedra placed inside an As_6 octahedron, which is in turn accommodated within an As_{12} cuboctahedron. The structure of the second

TABLE 6 | Selected interatomic distances in $Ba_8Ti_{13-x}M_xAs_{21}$ (M = Nb, Ta).

Atoms		Distance (Å)	
		$Ba_8Ti_{9.0(3)}Nb_{4.0}As_{21}$	$Ba_8Ti_{9.24(6)}Ta_{3.76}As_{21}$
Ba1	−As1 × 3	3.319 (2)	3.320 (1)
	−As3 × 3	3.3506 (6)	3.3515 (3)
	−As4	3.539 (1)	3.5430 (9)
	−As2 × 3	3.621 (2)	3.623 (1)
Ti/$M$1	−As3	2.467 (2)	2.473 (1)
	−As2 × 2	2.610 (1)	2.6102 (9)
	−As1 × 2	2.619 (2)	2.620 (1)
	−Ti/$M$1 × 4	3.078 (2)	3.075 (1)
	−Ti/$M$2	3.078 (2)	3.075 (1)
Ti/$M$2	−Ti/$M$1 × 12	3.078 (2)	3.075 (1)
As1	−As3 × 3	3.203 (2)	3.2043 (8)

nested polyhedron, located in the center of the unit cell, deviates from a regular γ-brass-type type cluster, and comprises an As_{12} cuboctahedron hosting a Ba_6 octahedron overlapped with an As_4 tetrahedron. The said Ba-Pn framework and a three-dimensional V scaffold are interpenetrated (**Figure 1B**). All V atoms are six-fold coordinated by the Pn atoms, and the resulting octahedra link by corner- and face-sharing and form a cage-like substructure (**Figure 1C**).

In all $Ba_5M_{12}Pn_{19+x}$ structures (M = Ti, V; Pn = As, Sb, Bi), partially occupied Pn sites are present in the central cuboctahedral cluster. However, the disorder pattern is strongly dependent on the transition metal and the pnictogen. In $Ba_5V_{12}As_{19.02(1)}$, extra As is located in the center of the unit cell (**Figure 1D**). The occupancy of this site refines to about 11 %. The adjacent Ba atoms in the corners of the octahedral shell show unphysically elongated thermal ellipsoids when refined as being positioned at a single crystallographic site. Splitting of this Ba position followed by independent refinement of the occupancies results in reasonable thermal parameters and occupation factors of about 89 and 11% for Ba1A and Ba1B, respectively. The splitting of Ba atom allows for two sets of distances to the center of the unit cell, where a partially occupied As atom (As6) is present −3.70 Å (Ba1A) and 3.33 Å (Ba1B), respectively. A good correlation of the Ba1B occupancy to that of the extra As site (As6) and the proximity of the total occupation of the two Ba atoms to unity implies the following account of the observed disorder: Whenever the As6 site is filled, the Ba_6 octahedron "shrinks" to optimize the chemical interactions. Indeed, the Ba1B–As6 distance corresponds well to the typical Ba–As bonding contacts (He et al., 2010; Wang et al., 2011). When the center of the unit cell is empty, the Ba atoms in the octahedron move farther apart, likely due to electrostatic repulsion and optimization of the remaining Ba–As bonds.

A very similar picture is observed in $Ba_5V_{12}Sb_{19.36(2)}$ (**Figure 1E**). In this case, the position in the center of the unit cell is 44% occupied by Sb (Sb6), and the corresponding splitting pattern of the adjacent Ba site indicates the same mechanism of structural relaxation to accommodate the extra Sb atom. In contrast to the arsenide, an additional Sb site (Sb7) is found
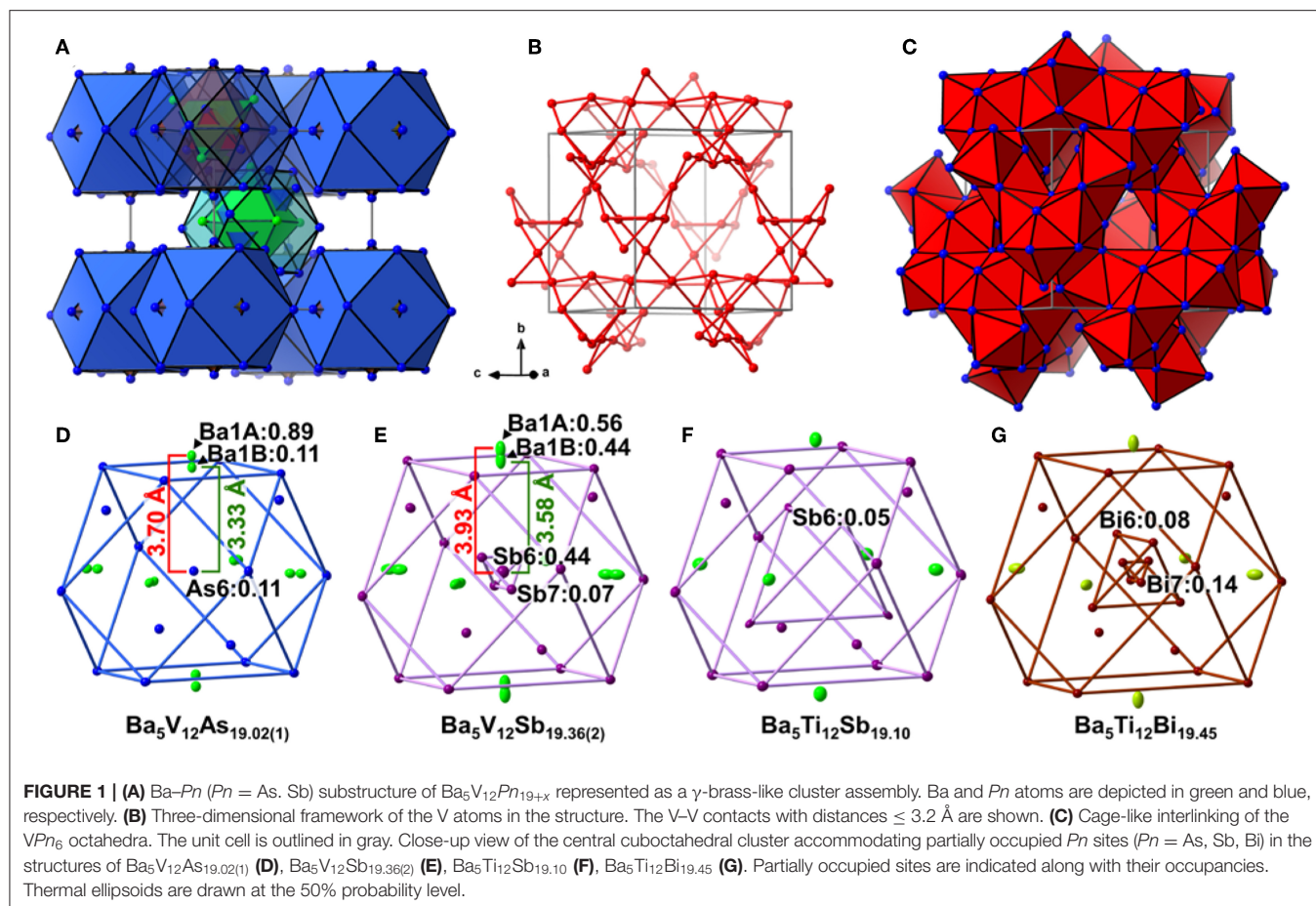
close to the unit cell center at a distance of 0.87(2) Å, giving rise to a split position with an occupancy of around 7 %. Due to short distances to the partially occupied Sb6 and Ba1B sites, this position can only reside in the octahedron composed of the Ba1A atoms, with no Sb in its center.

Interestingly, the realization of disorder is different in the $Ba_5Ti_{12}Sb_{19+x}$ and $Ba_5Ti_{12}Bi_{19+x}$. In the former case (**Figure 1F**), only one partially occupied Sb site is present in the structure (Bie and Mar, 2009). This Sb position (Sb6) is filled only 5% of the time (for the experimentally determined composition $Ba_5Ti_{12}Sb_{19.10}$) and is shifted from the center of the unit cell by 2.91 Å, forming a tetrahedron with an edge of 4.75 Å. Such a long interatomic separation renders any Sb6–Sb6 impossible. Yet a distance of 2.80 Å is observed between the Sb6 position and the Sb atoms on the triangular faces of the central cuboctahedral cluster, indicating covalent bonding. In $Ba_5Ti_{12}Bi_{19+x}$ (**Figure 1G**), there are two Bi sites with occupancies of about 8 and 14% (in $Ba_5Ti_{12}Bi_{19.45}$), which are shifted from the center of the unit cell by 1.85 Å (Bi6) and 0.54 Å (Bi7), respectively (Ovchinnikov and Bobev, 2018a). The Bi6 atoms form a tetrahedron with an edge of 3.01 Å inside the central cuboctahedral cluster. Substitution studies provide evidence that the occupancy of this site can be increased up to 25% for the approximate composition $SrEu_4Ti_{12}Bi_{20}$. This means that up to two Bi atoms can occupy the tetrahedron at a time, building a structural unit that is best viewed as a Bi_2 dumbbell (Ovchinnikov and Bobev, 2018a).

To sum up, the $Ba_5M_{12}Pn_{19+x}$ (M = Ti, V; Pn = As, Sb, Bi) compositions display very similar structures, but the subtle differences of the disorder pattern vary strongly with the transition metal and the pnictogen. The general trend which can be discerned from the side-by-side comparison of these structures, is the increasing degree of disorder upon going from the arsenides to the bismuthides. Apparently, the more compact structure of $Ba_5V_{12}As_{19.02(1)}$ is not able to accommodate additional interstitial atoms. Another factor to be considered here is the lower stability of polyanions containing heavier pnictogens, due to the decrease of electronegativity in the order As–Sb–Bi (Ovchinnikov and Bobev, 2019d). The latter factor may call for additional stabilization by homoatomic bonding in antimonides and bismuthides, which is realized upon accommodating some extra pnictogen sites in the structure. Disregarding the disordered sites, the Pn atoms in $Ba_5M_{12}Pn_{19+x}$ (M = Ti, V; Pn = As, Sb, Bi) may participate in hypervalent bonding, as suggested by some relatively short Pn–Pn contacts, e.g., 2.910(4) Å and 2.965(1) Å in $Ba_5V_{12}As_{19.02(1)}$, and 3.266(3) Å and 3.2252(9) Å in $Ba_5V_{12}Sb_{19.36(2)}$.

$Ba_8Ti_{13-x}M_xAs_{21}$ (M = Nb, Ta). The isostructural $Ba_8Ti_{13-x}Nb_xAs_{21}$ and $Ba_8Ti_{13-x}Ta_xAs_{21}$ adopt a new structure type with space group $Fm\bar{3}m$ and Pearson symbol $cF168$. The serendipitous incorporation of Nb and Ta metal from the crucible material into the structure, adds to many other instances of arsenides in particular (He et al., 2012; Baranets et al., 2018), where these typically high-melting and hard to activate elements prove to be quite reactive.

There are two symmetry-independent sites in the presented structures where the targeted transition metal atoms, Ti, and
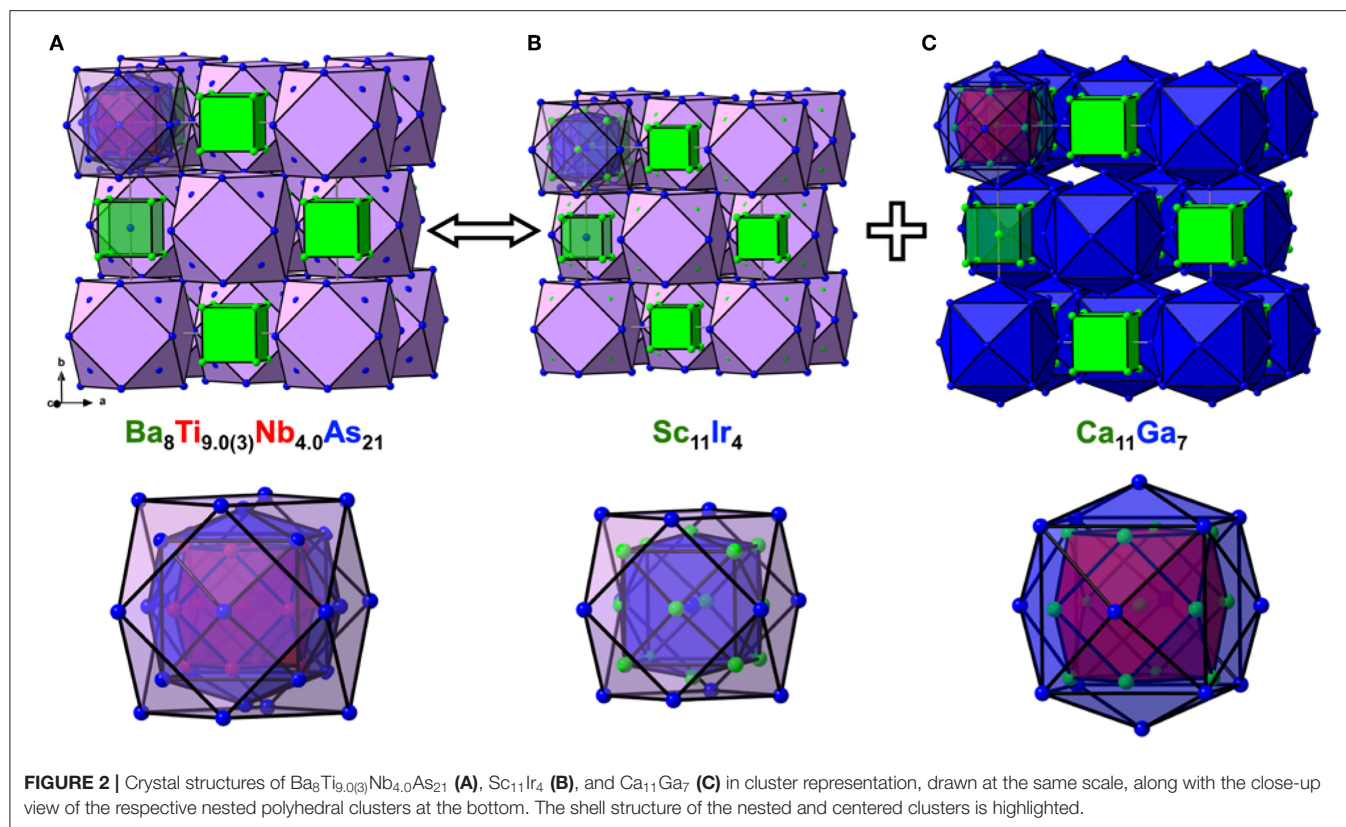
FIGURE 1 | (A) Ba–Pn (Pn = As. Sb) substructure of $Ba_5V_{12}Pn_{19+x}$ represented as a γ-brass-like cluster assembly. Ba and Pn atoms are depicted in green and blue, respectively. **(B)** Three-dimensional framework of the V atoms in the structure. The V–V contacts with distances ≤ 3.2 Å are shown. **(C)** Cage-like interlinking of the VPn_6 octahedra. The unit cell is outlined in gray. Close-up view of the central cuboctahedral cluster accommodating partially occupied Pn sites (Pn = As, Sb, Bi) in the structures of $Ba_5V_{12}As_{19.02(1)}$ **(D)**, $Ba_5V_{12}Sb_{19.36(2)}$ **(E)**, $Ba_5Ti_{12}Sb_{19.10}$ **(F)**, $Ba_5Ti_{12}Bi_{19.45}$ **(G)**. Partially occupied sites are indicated along with their occupancies. Thermal ellipsoids are drawn at the 50% probability level.

the atoms of group 5 element are found to be statistically mixed. These sites, hereafter referred to as $TM1$ and $TM2$ for brevity, are located in the vertices of a cuboctahedron and in its center, respectively, and account for isolated TM_{13} metal clusters (**Figure 2A**). The $TM1$–$TM1$ and $TM1$–$TM2$ distances are equal and measure $d_{TM-TM} = 3.078(2)$ Å and $3.075(1)$ Å for the Nb and Ta structures, respectively. The TM_{13} clusters can therefore be described as fragments of a perfect fcc-packing. The occurrence of such units is at first glance surprising, since the constituting transition metals form hexagonal close-packed (Ti) or bcc (Nb, Ta) structures at ambient conditions. A detailed account of the electronic interactions in the clusters will be given in the discussion of the electronic structure and chemical bonding (see below).

To simplify the description of the complex atomic arrangement in $Ba_8TM_{13}As_{21}$ and highlight relationships with other cubic metal-rich compounds, it is convenient to represent the structure as a packing of polyhedra, in a similar manner as was previously described for $Ba_5V_{12}Pn_{19+x}$. The $TM1$ sites are five-fold coordinated by As atoms, with the $TM2$ site completing a pseudo-octahedral coordination. The TM–As distances are very similar in both compounds and fall in the range 2.47–2.62 Å, in good agreement with the literature data on other titanium arsenides (Bachmayer et al., 1955; Nuss et al., 1996; Lee

et al., 2001). The basal As atoms of the pseudo-octahedra are located in the vertices of an As_{14} tetrakis hexahedron around the central $TM2$ atom, whereas the apical As atoms can be viewed as forming a regular As_{12} cuboctahedron around the same center. The described geometrical construction yields a nested four-shell polyhedron, $[TM2@TM1_{12}@As_{14}@As_{12/2}]$ ($=$ $TM_{13}As_{20}$), where the innermost "shell" is built up of a single atom. The notation "$As_{12/2}$" reflects the fact that each of the 12 As atoms in the outer cuboctahedral shell is shared between two symmetrically equivalent polyhedra. The shortest As–As distance in the structure is observed between the As atoms in the outermost and penultimate shells of the nested polyhedron and is found to be 3.203(2) Å and 3.2043(8) Å for the Nb and Ta representatives, respectively. The four-shell units form an fcc arrangement with the octahedral voids occupied by isolated As-centered $[AsBa_8]$ cubes.

The presented polyhedral description suggests that the structure of $Ba_8TM_{13}As_{21}$ can be thought of as a combination of the $Sc_{11}Ir_4$ (**Figure 2B**) and $Ca_{11}Ga_7$ (**Figure 2C**) structure types (Villars and Calvert, 1991). All three structures adopt space group $Fm\bar{3}m$ but show different populations of the Wyckoff sites. The nested polyhedron in $Sc_{11}Ir_4$, expressed as $[Ir@Sc_{14}@Ir_{12/2}]$, lacks the inner cuboctahedral shell, hosted by the similar unit in $Ba_8TM_{13}As_{21}$. The larger polyhedron

FIGURE 2 | Crystal structures of $Ba_8Ti_{9.0(3)}Nb_{4.0}As_{21}$ (A), $Sc_{11}Ir_4$ (B), and $Ca_{11}Ga_7$ (C) in cluster representation, drawn at the same scale, along with the close-up view of the respective nested polyhedral clusters at the bottom. The shell structure of the nested and centered clusters is highlighted.

in $Ca_{11}Ga_7$, on the contrary, accommodates a cuboctahedron, but represents a "peeled" version of the four-shelled cluster in the arsenide structure, with the following sequence of the shells: $[Ca@Ca_{12}@Ga_{14}]$. In both $Sc_{11}Ir_4$ and $Ca_{11}Ga_7$, centered cubes occupy the octahedral cavities in the *fcc* packing of the nested polyhedra.

The tetrahedral voids remain unoccupied in all three structures discussed above. Interestingly, in $Ba_8TM_{13}As_{21}$, the distance between the center of the tetrahedral hole to the nearest As atoms measures 2.355(2) Å and 2.358(1) Å in the Nb and Ta representatives, respectively. These numbers imply that it might be possible to intercalate a small metal atom into this cavity, which would result in a reasonable tetrahedral coordination and could change/augment the valence electron count, as discussed in the next section.
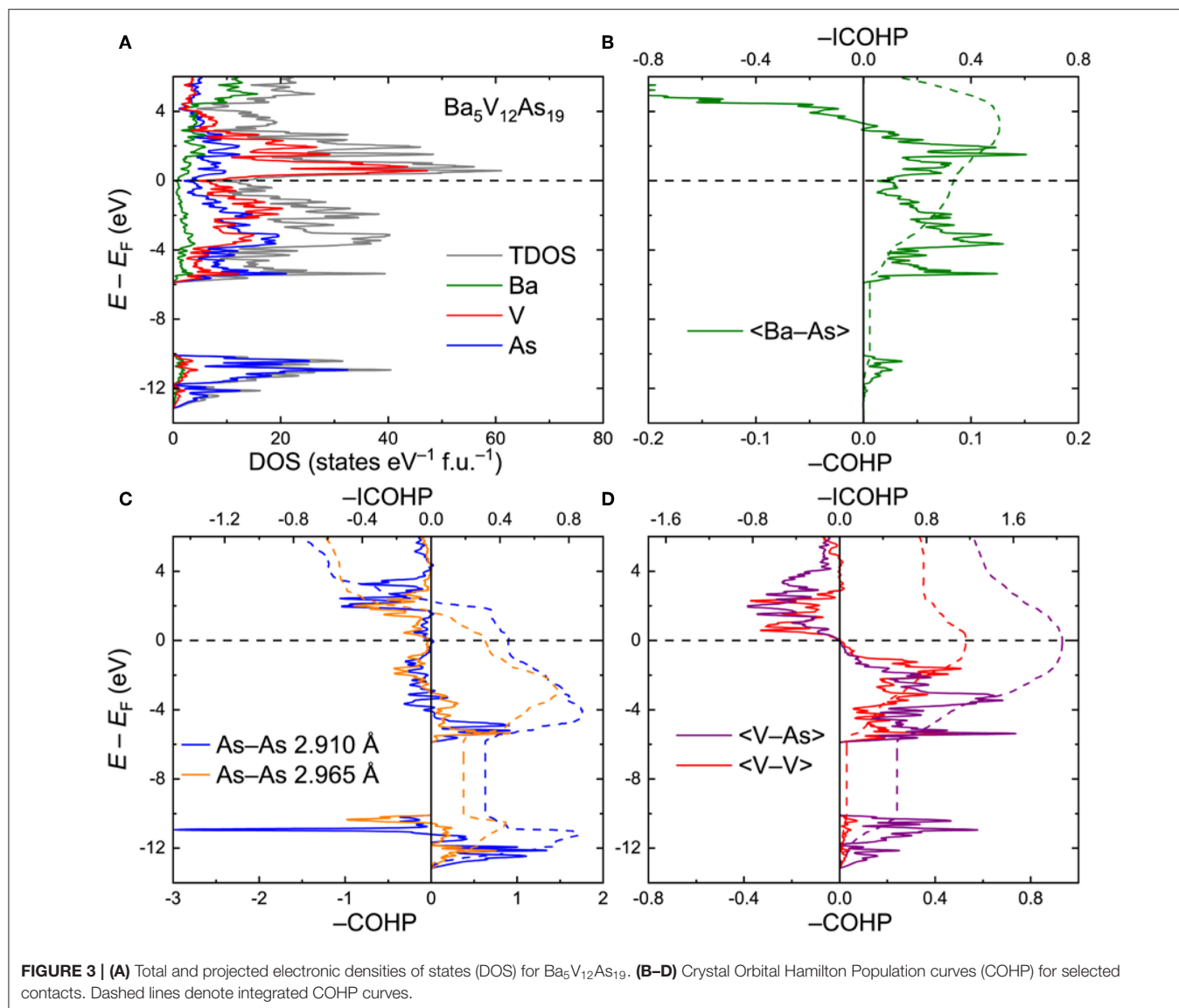
Electronic Structure

$Ba_5V_{12}As_{19}$. To interrogate the electronic structure and chemical bonding in the $Ba_5V_{12}Pn_{19+x}$ compounds, an idealized ordered $Ba_5V_{12}As_{19}$ model was utilized. Total and projected electronic densities of states (DOS) are shown in **Figure 3A**. The Fermi level (E_F) is located in the vicinity of a dip in the DOS: The electronic states close to E_F are primarily composed of the hybridized V(3d) and As(4p) orbitals. The Ba–As bonding deviates significantly from a simple ionic character as indicated by the sizeable continuous contribution of the Ba electronic states around the Fermi level. The As(4s) orbitals are highly localized in a narrow

energy interval around $E - E_F \approx -11$ eV. These states mainly manifest the presence of the As lone pairs in the structure.

Crystal Orbital Hamilton Population graphs (COHP) for average selected interatomic interactions are plotted in **Figures 3B–D**. In line with the conclusion derived from the projected DOS, the Ba–As interactions do not display a typical ionic nature. The bonding is underoptimized at E_F, with an energy window of unoccupied bonding states extending up to $E - E_F \approx 2.9$ eV (**Figure 3B**). The negative integrated COHP (–COHP) for the Ba–As amounts to about 0.34 eV/bond on average.

The two shortest As–As contacts demonstrate similar features in their COHP plots (**Figure 3C**). Both contacts are characterized by a combination of bonding and antibonding states below E_F. The resulting attractive interaction is rather weak, yet the –ICOHP values of 0.31 and 0.45 eV/bond for the longer and shorter As–As contacts, respectively, are comparable with the numbers found for the Ba–As bonds. Altogether, the observed COHP pattern for the As–As contacts is in accordance with hypervalent (electron-rich) chemical bonding (Papoian and Hoffmann, 2000; Ovchinnikov and Bobev, 2018b,c).

In contrast, the V–As and V–V bonds are optimized at the Fermi level, with the respective average –ICOHP magnitudes of 2.05 and 1.16 eV/bond (**Figure 3D**). It is worth noting that in $Ba_5V_{12}As_{19}$, only a small number of V–As and V–V bonding states are available in the near vicinity of E_F down to $E - E_F \approx -1.2$ eV. This energy may correspond to the lowest electron count which would retain the structural stability. Indeed, upon

FIGURE 3 | (A) Total and projected electronic densities of states (DOS) for $Ba_5V_{12}As_{19}$. **(B–D)** Crystal Orbital Hamilton Population curves (COHP) for selected contacts. Dashed lines denote integrated COHP curves.
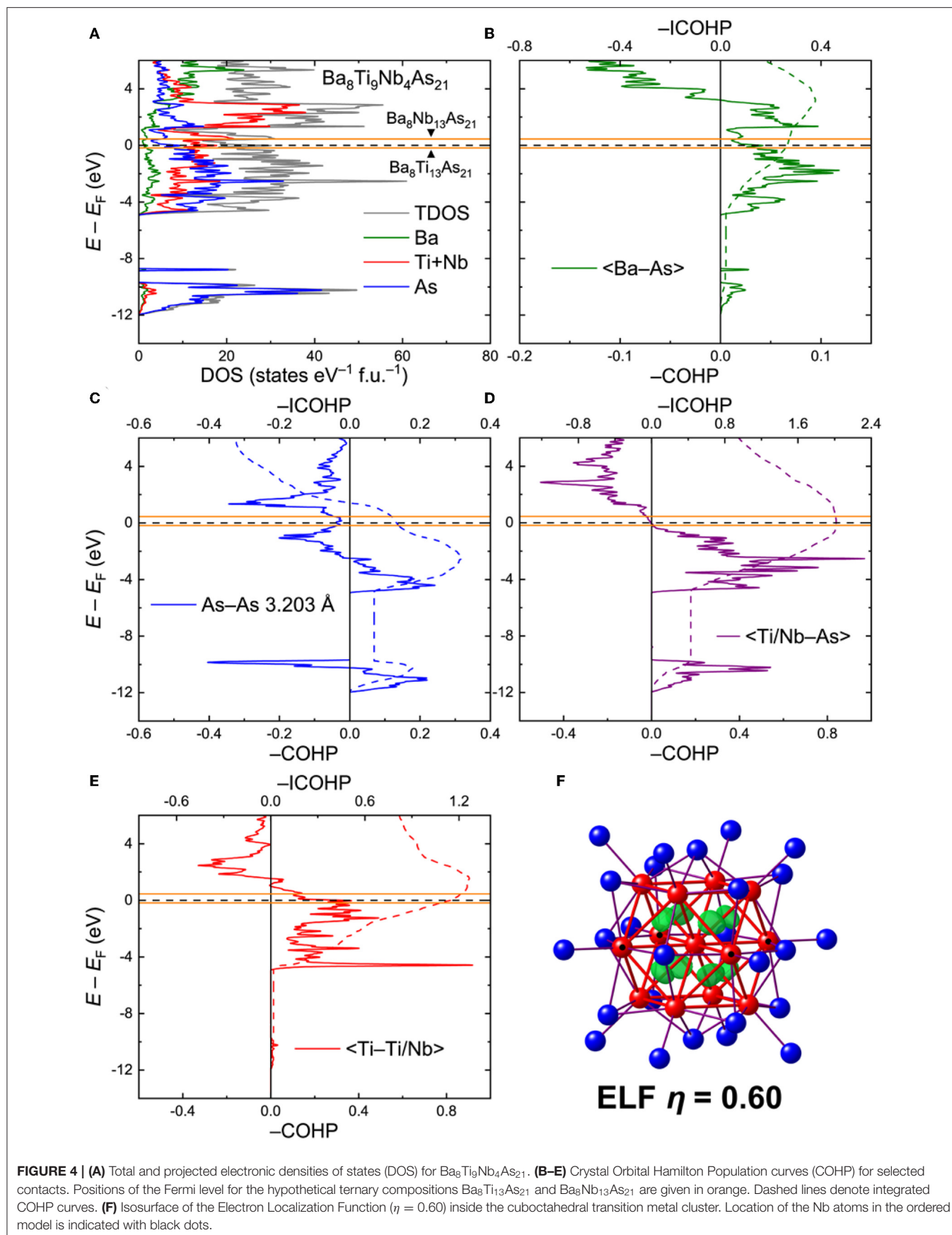
lowering the Fermi level by more than 1.2 eV, the bonding V–As and V–V states get progressively vacated, perturbing the respective bonding. Introduction of small amounts of extra As, as in the experimentally determined composition $Ba_5V_{12}As_{19.02(1)}$, can be viewed as a mild oxidation of the discussed $Ba_5V_{12}As_{19}$ composition and will have a very small effect on the V–As and V–V bonds. Furthermore, the hitherto unknown $Ba_5Ti_{12}As_{19}$ would also fall in the stability region according to the suggested electronic considerations. If a rigid band model can be applied in this case, the electronic structure of $Ba_5Ti_{12}As_{19}$ can be derived from that of $Ba_5V_{12}As_{19}$ by shifting the Fermi level down by about 0.89 eV, which would correspond to removal of 12 electrons per formula unit with respect to the vanadium composition. In fact, the resulting hypothetical electronic structure would tolerate even further oxidation, e.g., by incorporation of extra pnictogen atoms. This prediction suggests that the apparent non-existence (or lower stability) of $Ba_5Ti_{12}As_{19+x}$ does not originate from

electronic reasons. Atomic size factors or peculiarities of the reaction pathways in the Ba–Ti–As system should be examined in detail to resolve this conundrum.

$Ba_8Ti_9Nb_4As_{21}$. For analysis of the electronic interactions in the $Ba_8Ti_{13-x}M_xAs_{21}$ phases (M = Nb, Ta), an ordered model with composition $Ba_8Ti_9Nb_4As_{21}$ was generated. The electronic density of states (DOS) for this model is given in **Figure 4A**. In contrast to the $Ba_5V_{12}As_{19}$ case, the Fermi level in $Ba_8Ti_9Nb_4As_{21}$ crosses a peak in the DOS, mainly composed of the transition metal d orbitals. The high density of states may indicate some electronic instabilities, warranting further experimental studies. In this respect, it is worthwhile to note that spin-polarized calculations did not indicate any localized magnetism, rendering magnetic instability quite improbable.

The calculated COHP curves for averaged selected contacts in the structure are presented in **Figures 4B–E**. For the sake of simplicity, the contacts involving Ti and

FIGURE 4 | (A) Total and projected electronic densities of states (DOS) for $Ba_8Ti_9Nb_4As_{21}$. **(B–E)** Crystal Orbital Hamilton Population curves (COHP) for selected contacts. Positions of the Fermi level for the hypothetical ternary compositions $Ba_8Ti_{13}As_{21}$ and $Ba_8Nb_{13}As_{21}$ are given in orange. Dashed lines denote integrated COHP curves. **(F)** Isosurface of the Electron Localization Function ($\eta = 0.60$) inside the cuboctahedral transition metal cluster. Location of the Nb atoms in the ordered model is indicated with black dots.

Nb in the ordered model were averaged. The Ba–As interactions bear resemblance to the respective contacts in $Ba_5V_{12}As_{19}$, with somewhat underoptimized bonding at E_F (**Figure 4B**). The average –ICOHP value for these contacts is 0.27 eV/bond.

The shortest As–As contact, despite a considerable interatomic separation, displays a non-negligible, yet underoptimized, bonding interaction, with a domain of occupied antibonding states just below E_F (**Figure 4C**), akin to $Ba_5V_{12}As_{19}$. In an idealized picture, these bonds can be treated as one-electron interactions (Papoian and Hoffmann, 2000). This very crude approximation allows assignment of formal charges to the As sites. An isolated As atom (i.e., with no short As–As contacts) has a formal charge of 3–, whereas every one-electron bond lowers the absolute negative charge by 0.5. In terms of such one-electron bonds, the As atoms in $Ba_8Ti_9Nb_4As_{21}$ are either isolated or three- and four-fold coordinated. The schematic representation of the As framework is shown in **Figure S1**. In the limit of full electron localization, the formula can be expressed as $(Ba^{2+})_8[Ti_9Nb_4]^{23+}(As^{3-})_7(As^{1.5-})_8(As^{1-})_6$. Although this electronic distribution is an oversimplification, it will provide an insight into the metal-metal bonding in the clusters, as discussed below.

Quite notably, the transition-metal–arsenic bonds are perfectly optimized at the Fermi level (**Figure 4D**). The strong covalent nature of these bonds is evident from the high average—ICOHP magnitude of 2.02 eV/bond. Similarly to $Ba_5V_{12}As_{19}$, the number of the occupied bonding states just below E_F and the vacant antibonding states close to E_F is rather small, suggesting that moderate changes in the electron count would not strongly affect the bonding. In particular, shifting the Fermi level down by 0.17 eV or lifting it up by 0.45 eV, corresponding to the positions of E_F in the hypothetical $Ba_8Ti_{13}As_{21}$ and $Ba_8Nb_{13}As_{21}$, respectively (orange lines in **Figure 4**), will have virtually no influence on the transition-metal–arsenic interactions.

The situation is different for the metal–metal bonds, which appear to be underoptimized for the composition $Ba_8Ti_9Nb_4As_{21}$, owing to the availability of unoccupied bonding states above E_F (**Figure 4E**). These states extend up to $E - E_F \approx 1.54$ eV, which would correspond to ~35 extra electrons per formula unit. This finding shows that electron doping in $Ba_8Ti_9Nb_4As_{21}$ is favorable and expected to enhance the metal-metal interactions, which are already quite strong for the examined composition, with an average –ICOHP of 1.14 eV/bond. The maximum –ICOHP value that can be achieved by filling up all the bonding states above E_F amounts to 1.26 eV/bond. At this high electron count, however, some occupation of the antibonding transition-metal–arsenic states will be attained. Since the structure is dominated by the latter kind of bonds in terms of their number and relative strength, it is likely that these bonds will be pivotal for the overall stability.

Analysis of the Electron Localization Function (ELF) for the Ba–As contacts did not reveal any localization maxima but indicated small deviation of the ELF distribution from a spherical shape around the atoms, typical for highly polar bonds. A much more pronounced deviation was found for the *TM*–As contacts (**Figure S2a**). Increased values and flattening of the ELF was also observed for the short As–As contacts (**Figure S2b**). Clear localization domains are visible inside the tetrahedral voids of the cuboctahedral cluster, suggesting multi-center metal–metal bonding (**Figure 4F**). Detailed inspection of the ELF sections revealed the presence of additional ELF maxima on the lines connecting the central transition metal atom to the twelve vertices of the cuboctahedron, indicating two-center bonds (**Figure S2c**). In a very naïve picture of perfect electron localization, the formation of eight multi-center and 12 two-center bonds would require 40 electrons in total, if all these bonds are treated as two-electron. By considering the formula derived above, $(Ba^{2+})_8[Ti_9Nb_4]^{23+}(As^{3-})_7(As^{1.5-})_8(As^{1-})_6$, the total number of valence electrons inside the $[Ti_9Nb_4]$ cluster is $9 \times 4 + 4 \times 5 - 23 = 33$. The limiting hypothetical compositions $Ba_8Ti_{13}As_{21}$ and $Ba_8Nb_{13}As_{21}$ would correspond to 29 and 42 cluster electrons, respectively. The proposed simple electron accounting is in line with the conclusion that electron doping of $Ba_8Ti_9Nb_4As_{21}$ will stabilize the bonding inside the clusters. A more accurate approach of determining the number of cluster electrons is direct integration of electron density inside the Bader basins of the transition metal atoms. This method yields 37.92 electrons in the $[Ti_9Nb_4]$ cluster, which is somewhat below the optimal number obtained by the overly-simplified electron counting above. Since the bonding in the metallic $Ba_8Ti_9Nb_4As_{21}$ is rather delocalized, the valence electron considerations detailed above should be deemed a *qualitative* rationale for the stability of the discussed complex crystal structure. It seems very likely that $Ba_8Ti_9Nb_4As_{21}$ will show some flexibility with respect to the total electron count and definitely requires a more detailed experimental examination.

CONCLUSIONS

The metal flux method is a powerful approach for crystal growth of various kinds of intermetallic compounds. Its simple design and wide applicability makes it an efficient tool for exploratory synthetic research. Two ternary barium vanadium pnictides, $Ba_5V_{12}As_{19.02(1)}$ and $Ba_5V_{12}Sb_{19.36(2)}$ were successfully grown as mm-sized single crystals employing selected flux materials—Pb and Sb, respectively. The crystal structure of both compounds can be described as γ-brass-like cluster assemblies based on Ba and *Pn* (*Pn* = As, Sb), interpenetrated by three-dimensional V scaffolds. The observed non-stoichiometry results from additional partially occupied *Pn* positions, which show different disorder patterns depending on the pnictogen. First-principle calculations predict high flexibility of the structure with respect to the electron count, which explains the existence of the related electron-poorer Ti phases $Ba_5Ti_{12}Sb_{19+x}$ and $AE_5Ti_{12}Bi_{19+x}$ (*AE* = Sr, Ba). Following the analogy between the V and Ti pnictides, we attempted to obtain the hitherto unknown $Ba_5Ti_{12}As_{19+x}$, employing the flux technique and conventional high-temperature annealing of the elements in metal tubes. The latter approach yielded two new compounds, $Ba_8Ti_{9.0(3)}Nb_{4.0}As_{21}$ and $Ba_8Ti_{9.24(6)}Ta_{3.76}As_{21}$, as a result of

side-reactions with the container material. The quaternary compositions crystallize isotypically in a new structure type, which displays isolated *fcc*-type clusters composed of statistically mixed Ti and *M* atoms (*M* = Nb, Ta). First-principle calculations reveal that the bonding within these units displays two-center and multi-center features and complex electron distribution. The presented examples demonstrate that the field of early transition metal pnictides deserves additional study, as many new compounds with potentially interesting structures and properties are likely to be found. In this respect, the flux method proves to be a handy tool for exploration of these systems.

DATA AVAILABILITY STATEMENT

The datasets generated for this study can be found in the The Cambridge Crystallographic Data Centre (CCDC) under the deposition numbers 1959265-1959268.

AUTHOR CONTRIBUTIONS

AO designed and carried out the synthesis, performed crystallographic characterization and first-principle calculations, and prepared the initial draft of the manuscript. SB supervised the project and finalized the manuscript.

FUNDING

SUPPLEMENTARY MATERIAL

The Supplementary Material for this article can be found online at: https://www.frontiersin.org/articles/10.3389/fchem.2019.00909/full#supplementary-material

REFERENCES

Bachmayer, K., Nowotny, H., and Kohl, A. (1955). Die Struktur von TiAs. *Monatsh. Chem.* 86, 39–43. doi: 10.1007/BF00899271

Bao, J.-K., Bugaris, D. E., Zheng, H., Willa, K., Welp, U., Chung, D. Y., et al. (2019). Superconductivity in $Y_7Ru_4InGe_{12}$. *Phys Rev Mater.* 3:024802. doi: 10.1103/PhysRevMaterials.3.024802

Bao, J.-K., Liu, J.-Y., Ma, C.-W., Meng, Z.-H., Tang, Z.-T., Sun, Y.-L., et al. (2015). Superconductivity in quasi-one-dimensional $K_2Cr_3As_3$ with significant electron correlations. *Phys. Rev. X.* 5:011013. doi: 10.1103/PhysRevX.5.011013

Baranets, S., and Bobev, S. (2019). From the ternary phase $Ca_{14}Zn_{1+\delta}Sb_{11}$ ($\delta \approx 0.4$) to the quaternary solid solutions $Ca_{14-x}RE_xZnSb_{11}$ (RE = La–Nd, Sm, Gd, $x \approx 0.9$). A tale of electron doping via rare-earth metal substitutions and the concomitant structural transformations. *Inorg. Chem.* 58, 8506–8516. doi: 10.1021/acs.inorgchem.9b00809

Baranets, S., Darone, G. M., and Bobev, S. (2019a). Synthesis and structure of $Sr_{14}Zn_{1+x}As_{11}$ and $Eu_{14}Zn_{1+x}As_{11}$ ($x \leq 0.5$). New members of the family of pnictides isotypic with $Ca_{14}AlSb_{11}$, exhibiting a new type of structural disorder. *J. Solid. State. Chem.* 280:120990. doi: 10.1016/j.jssc.2019.120990

Baranets, S., He, H., and Bobev, S. (2018). Niobium-bearing arsenides and germanides from elemental mixtures not involving niobium: a new twist to an old problem in solid-state synthesis. *Acta. Crystallogr. C.* 74, 623–627. doi: 10.1107/S2053229618005739

Baranets, S., Voss, L., Stoyko, S., and Bobev, S. (2019b). Synthesis, crystal structure and physical properties of the solid solutions $Ca_{14-x}RE_xCdSb_{11}$ (RE = La–Nd, Sm, Gd–Yb, $x \approx 0.85 \pm 0.15$). *J. Appl. Phys.* 125:245101. doi: 10.1063/1.5099632

Bie, H., and Mar, A. (2009). $Ba_5Ti_{12}Sb_{19+x}$, a polar intermetallic compound with a stuffed γ-brass structure. *J. Solid. State. Chem.* 182, 3131–3137. doi: 10.1016/j.jssc.2009.08.030

Brylak, M., and Jeitschko, W. (1994). U_3TiSb_5, U_3VSb_5, U_3CrSb_5, and U_3MnSb_5 with 'Anti'-Hf_5Sn_3Cu Type Structure. *Z Naturforsch. B.* 49, 747–752. doi: 10.1515/znb-1994-0605

Canfield, P. C., and Fisk, Z. (1992). Growth of single crystals from metallic fluxes. *Philos. Mag. B.* 65, 1117–1123. doi: 10.1080/13642819208215073

Chen, L., and Corbett, J. D. (2004). $R_6TT'_2$, New variants of the Fe_2P structure type. Sc_6TTe_2 (T = Ru, Os, Rh, Ir), Lu_6MoSb_2, and the anti-typic $Sc_6Te_{0.80}Bi_{1.68}$. *Inorg. Chem.* 43, 436–442. doi: 10.1021/ic0302581

Childs, A. B., Baranets, S., and Bobev, S. (2019). Five new ternary indium-arsenides discovered. Synthesis and structural characterization of the Zintl phases $Sr_3In_2As_4$, $Ba_3In_2As_4$, $Eu_3In_2As_4$, $Sr_5In_2As_6$ and $Eu_5In_2As_6$. *J. Solid. State. Chem.* 278:120889. doi: 10.1016/j.jssc.2019.07.050

Doan, P., Gooch, M., Tang, Z., Lorenz, B., Möller, A., Tapp, J., et al. (2012). $Ba_{1-x}Na_xTi_2Sb_2O(0.0 \leq x \leq 0.33)$: a layered titanium-based pnictide oxide superconductor. *J. Am. Chem. Soc.* 134, 16520–16523. doi: 10.1021/ja3078889

Failamani, F., Grytsiv, A., Giester, G., Polt, G., Heinrich, P., Michor, H., et al. (2015). $Ba_5\{V,Nb\}_{12}Sb_{19+x}$, novel variants of the $Ba_5Ti_{12}Sb_{19+x}$-type: crystal structure and physical properties. *Phys. Chem. Chem. Phys.* 17, 24248–24261. doi: 10.1039/C5CP04000K

Felder, J. B., Weiland, A., Hodovanets, H., McCandless, G. T., Estrada, T. G., Martin, T. J., et al. (2019). Law and disorder: special stacking units—building the intergrowth $Ce_6Co_5Ge_{16}$. *Inorg. Chem.* 58, 6037–6043. doi: 10.1021/acs.inorgchem.9b00350

Gelato, L. M., and Parthé, E. (1987). *STRUCTURE TIDY* – a computer program to standardize crystal structure data. *J. Appl. Crystallogr.* 20, 139–143. doi: 10.1107/S0021889887086965

Han, F., Bao, J.-K., Malliakas, C. D., Sturza, M., Du, Y., Chung, D. Y., et al. (2019). Enormous electron-electron scattering in the filled-cage cubic compound $Ba_{10}Ti_{24}Bi_{39}$. *Phys. Rev. Mater.* 3:105001. doi: 10.1103/PhysRevMaterials.3.105001

He, H., Stearrett, R., Nowak, E. R., and Bobev, S. (2010). $BaGa_2Pn_2$ (Pn = P, As): New semiconducting phosphides and arsenides with layered structures. *Inorg. Chem.* 49, 7935–7940. doi: 10.1021/ic100940b

He, H., Tyson, C., and Bobev, S. (2012). Synthesis and crystal structures of the quaternary zintl phases $RbNa_8Ga_3Pn_6$ (Pn = P, As) and $Na_{10}NbGaAs_6$. *Crystals* 2, 213–223. doi: 10.3390/cryst2020213

Jayasinghe, A. S., Lai, Y., Baumbach, R., and Latturner, S. E. (2019). $U_{1.33}T_4Al_8Si_2$ (T = Ni, Co): complex uranium silicides grown from aluminum/gallium flux mixtures. *Inorg. Chem.* 58, 12209–12217. doi: 10.1021/acs.inorgchem.9b01627

Jepsen, O., and Andersen, O. K. (2000). *The Stuttgart TB-LMTO-ASA Program, Version 4.7; Max-Planck-Institut für Festkörperforschung.* Stuttgart.

Kanatzidis, M. G., Pöttgen, R., and Jeitschko, W. (2005). The metal flux: a preparative tool for the exploration of intermetallic compounds. *Angew. Chem. Int. Ed.* 44, 6996–7023. doi: 10.1002/anie.200462170

Khan, M. A., McCandless, G. T., Benavides, K. A., Martin, T. J., Palacios, A. M., Samuel, A. W. B., et al. (2018). Crystal Growth and Magnetic Properties of $Pr_3Co_{2+x}Ge_7$ and the Sn-Stabilized $Ln_3Co_{2+x}Ge_{7-y}Sn_y$ (Ln = Pr, Nd, Sm). *Cryst. Growth. Des.* 18, 6028–6034. doi: 10.1021/acs.cgd.8b00868

Latturner, S. E. (2018). Clusters, assemble: growth of intermetallic compounds from metal flux reactions. *Acc. Chem. Res.* 51, 40–48. doi: 10.1021/acs.accounts.7b00483

Lee, C. S., Dashjav, E., and Kleinke, H. (2001). Structure prediction using our semiempirical structure map: the crystal structure of the new arsenide ZrTiAs. *Chem. Mater.* 13, 4053–4057. doi: 10.1021/cm010433g

Ma, X., Chen, B., and Latturner, S. E. (2012). Synthesis and properties of new multinary silicides $R_5Mg_5Fe_4Al_xSi_{18-x}$ (R = Gd, Dy, Y, $x \approx 12$) grown in Mg/Al Flux. *Inorg. Chem.* 51, 6089–6095. doi: 10.1021/ic202735b

Nakamura, S., Kano, T., and Ohara, S. (2019). Magnetic ordering in kondo lattice compound $YbIr_3Si_7$. *J. Phys. Soc. Jpn.* 88:093705. doi: 10.7566/JPSJ.88.093705

Nuss, J., Hönle, W., Peters, K., and Schnering, H. G. V. (1996). Tetrapnictidotitanate(IV) M_4TiX_4 (M = Sr, Ba; X = P, As), hierarchische Derivate der KGe-Struktur $K_4\square Ge_4$. *Z. Anorg. Allg. Chem.* 622, 1879–1885. doi: 10.1002/zaac.19966221112

Otero-de-la-Roza, A., Johnson, E. R., and Luaña, V. (2014). Critic2: a program for real-space analysis of quantum chemical interactions in solids. *Comput. Phys. Commun.* 185, 1007–1018. doi: 10.1016/j.cpc.2013.10.026

Ovchinnikov, A., and Bobev, S. (2018a). Synthesis, crystal and electronic structure of the titanium bismuthides $Sr_5Ti_{12}Bi_{19+x}$, $Ba_5Ti_{12}Bi_{19+x}$, and $Sr_{5-\delta}Eu_\delta Ti_{12}Bi_{19+x}$ ($x \approx 0.5$–1.0; $\delta \approx 2.4$, 4.0). *Eur. J. Inorg. Chem.* 2018, 1266–1274. doi: 10.1002/ejic.201701426

Ovchinnikov, A., and Bobev, S. (2018b). On the effect of Ga and In substitutions in the $Ca_{11}Bi_{10}$ and $Yb_{11}Bi_{10}$ bismuthides crystallizing in the tetragonal $Ho_{11}Ge_{10}$ structure type. *Acta. Crystallogr. C.* 74, 269–273. doi: 10.1107/S2053229618001596

Ovchinnikov, A., and Bobev, S. (2018c). Undistorted linear Bi chains with hypervalent bonding in La_3TiBi_5 from single-crystal X-ray diffraction. *Acta. Crystallogr. C.* 74, 618–622. doi: 10.1107/S205322961800565X

Ovchinnikov, A., and Bobev, S. (2019a). Multifaceted Sn–Sn bonding in the solid state. Synthesis and structural characterization of four new Ca–Li–Sn compounds. *Dalton. Trans.* 48, 14398–14407. doi: 10.1039/C9DT02803J

Ovchinnikov, A., and Bobev, S. (2019b). Synthesis, and crystal and electronic structures, of the titanium-rich bismuthides $AE_3Ti_8Bi_{10}$ (AE = Sr, Ba, Eu). *Inorg. Chem.* 58, 2934–2941. doi: 10.1021/acs.inorgchem.8b01952

Ovchinnikov, A., and Bobev, S. (2019c). Layered quaternary germanides— synthesis and crystal and electronic structures of $AELi_2In_2Ge_2$ (AE = Sr, Ba, Eu). *Inorg. Chem.* 58, 7895–7904. doi: 10.1021/acs.inorgchem.9b00588

Ovchinnikov, A., and Bobev, S. (2019d). Zintl phases with group 15 elements and the transition metals: a brief overview of pnictides with diverse and complex structures. *J.Solid. State. Chem.* 270, 346–359. doi: 10.1016/j.jssc.2018.11.029

Ovchinnikov, A., and Bobev, S. (2020). Bismuth as a reactive solvent in the synthesis of multicomponent transition-metal-bearing bismuthides. *Inorg. Chem.* doi: 10.1021/acs.inorgchem.9b02881. [Epub ahead of print].

Ovchinnikov, A., Darone, G., Saparov, B., and Bobev, S. (2018a). Exploratory work in the quaternary system of Ca–Eu–Cd–Sb: synthesis, crystal, and electronic structures of new zintl solid solutions. *Materials* 11:2146. doi: 10.3390/ma11112146

Ovchinnikov, A., Makongo, J. P. A., and Bobev, S. (2018b). Yet again, new compounds found in systems with known binary phase diagrams. Synthesis, crystal and electronic structure of Nd_3Bi_7 and Sm_3Bi_7. *Chem. Commun.* 54, 7089–7092. doi: 10.1039/C8CC02563K

Ovchinnikov, A., Prakash, J., and Bobev, S. (2017a). Crystal chemistry and magnetic properties of the solid solutions $Ca_{14-x}RE_xMnBi_{11}$ (RE = La–Nd, Sm, and Gd–Ho; $x \approx 0.6$–0.8). *Dalton. Trans.* 46, 16041–16049. doi: 10.1039/C7DT03715E

Ovchinnikov, A., Saparov, B., Xia, S.-Q., and Bobev, S. (2017b). The ternary alkaline-earth metal manganese bismuthides Sr_2MnBi_2 and $Ba_2Mn_{1-x}Bi_2$ ($x \approx 0.15$). *Inorg. Chem.* 56, 12369–12378. doi: 10.1021/acs.inorgchem.7b01851

Papoian, G., and Hoffmann, R. (2000). Hypervalent bonding in one, two, and three dimensions: extending the Zintl-Klemm concept to nonclassical electron-rich networks. *Angew. Chem. Int. Ed.* 39, 2408–2448. doi: 10.1002/1521-3773(20000717)39:14<2408::AID-ANIE2408>3.0.CO;2-U

Raju, N. P., Greedan, J. E., Ferguson, M. J., and Mar, A. (1998). $LaCrSb_3$: a new itinerant electron ferromagnet with a layered structure. *Chem. Mater.* 10, 3630–3635. doi: 10.1021/cm9803758

SADABS (2014). Bruker AXS Inc. Madison, WI: SADABS

SAINT (2014). Bruker AXS Inc. Madison, WI: SAINT.

Savin, A., Nesper, R., Wengert, S., and Fässler, T. F. (1997). ELF: the electron localization function. *Angew Chem Int Ed Engl.* 36, 1808–1832. doi: 10.1002/anie.199718081

Sheldrick, G. M. (2015a). *SHELXT* – Integrated space-group and crystal-structure determination. *Acta. Crystallogr. A.* 71, 3–8. doi: 10.1107/S2053273314026370

Sheldrick, G. M. (2015b). Crystal structure refinement with *SHELXL*. *Acta. Crystallogr. C.* 71, 3–8. doi: 10.1107/S2053229614024218

Steinberg, S., and Dronskowski, R. (2018). The Crystal Orbital Hamilton Population (COHP) method as a tool to visualize and analyze chemical bonding in intermetallic compounds. *Crystals* 8:225. doi: 10.3390/cryst8050225

Villars, P., and Calvert, L. D. (1991). *Pearson's Handbook of Crystallographic Data for Intermetallic Phases*, 2nd Edn. Materials Park, OH: American Society for Metals.

von Barth, U., and Hedin, L. (1972). A local exchange-correlation potential for the spin polarized case: I. *J. Phys. C. Solid. State. Phys.* 5, 1629–1642. doi: 10.1088/0022-3719/5/13/012

Wakiya, K., Sugiyama, Y., Komagata, T., Uehara, M., Sato, H., Gouchi, J., et al. (2019). Intermediate valence state of Ce in the novel quaternary compound $CeRu_2Sn_2Zn_{18}$. *J. Alloys. Compd.* 797, 309–313. doi: 10.1016/j.jallcom.2019.04.345

Wang, J., Yang, M., Pan, M.-Y., Xia, S.-Q., Tao, X.-T., He, H., et al. (2011). Synthesis, crystal and electronic structures, and properties of the new pnictide semiconductors A_2CdPn_2 (A = Ca, Sr, Ba, Eu; Pn = P, As). *Inorg. Chem.* 50, 8020–8027. doi: 10.1021/ic200286t

Wolff, G. A., and Mlavsky, A. I. (1974). "Travelling solvent techniques," in *Crystal Growth: Theory and Techniques,* Vol. 1, ed C. H. L. Goodman (Boston, MA: Springer US), 193–232.

Zaikina, J. V., Griffin, V. S., and Latturner, S. E. (2017). Switching on a spin glass: flux growth, structure, and magnetism of $La_{11}Mn_{13-x-y}Ni_xAl_ySn_{4-\delta}$ intermetallics. *Inorg. Chem.* 56, 15194–15202. doi: 10.1021/acs.inorgchem.7b02555

Zaikina, J. V., Jo, Y.-J., and Latturner, S. E. (2010). Ruthenium intermetallics grown from La–Ni Flux: synthesis, structure, and physical properties. *Inorg. Chem.* 49, 2773–2781. doi: 10.1021/ic902151d